1   Tropical Continental Downdraft Characteristics: Mesoscale Systems versus Unorganized

2   Convection

3   Kathleen A. Schiro[1] and J. David Neelin[1]

4   [1]*Department of Atmospheric and Oceanic Sciences, University of California Los Angeles, Los*

5   *Angeles, CA, USA*

6   Corresponding Author: Kathleen A. Schiro, Department of Atmospheric and Oceanic Sciences,

7   University of California, Los Angeles, Box 951565, Los Angeles, CA 90095. E-mail:

8   kschiro@atmos.ucla.edu

10   **Abstract**

11   Downdrafts and cold pool characteristics for strong mesoscale convective systems

12   (MCSs) and isolated, unorganized deep precipitating convection are analyzed using multi-

13   instrument data from the DOE Atmospheric Radiation Measurement (ARM) GoAmazon2014/5

14   campaign. Increases in column water vapor (CWV) are observed leading convection, with higher

15   CWV preceding MCSs than for isolated cells. For both MCSs and isolated cells, increases in

16   wind speed, decreases in surface moisture and temperature, and increases in relative humidity

17   occur coincidentally with system passages. Composites of vertical velocity data and radar

18   reflectivity from a radar wind profiler show that the downdrafts associated with the sharpest

19   decreases in surface equivalent potential temperature (θ_e) have a probability of occurrence that

20   increases with decreasing height below the freezing level. Both MCSs and unorganized

21   convection show similar mean downdraft magnitudes and probabilities with height. Mixing

22   computations suggest that, on average, air originating at heights greater than 3 km must undergo

23   substantial mixing, particularly in the case of isolated cells, to match the observed cold pool θ_e,

24   implying a low typical origin level. Precipitation conditionally averaged on decreases in surface

25   equivalent potential temperature ($\Delta\theta_e$) exhibits a strong relationship because the most negative

26   $\Delta\theta_e$ values are associated with a high probability of precipitation. The more physically motivated

27   conditional average of $\Delta\theta_e$ on precipitation shows that decreases in θ_e level off with increasing

28   precipitation rate, bounded by the maximum difference between surface θ_e and its minimum in

29 the profile aloft. Robustness of these statistics observed across scales and regions suggests their

30 potential use as model diagnostic tools for the improvement of downdraft parameterizations in

31 climate models.

32 1 Introduction

33   Convective downdrafts involve complex interactions between dynamics,

34 thermodynamics, and microphysics across scales. They form cold pools, which are evaporatively

35 cooled areas of downdraft air that spread horizontally and can initiate convection at their leading

36 edge (Byers and Braham 1949; Purdom 1976; Wilson and Schreiber 1986; Rotunno et al. 1988;

37 Fovell and Tan 1998; Tompkins 2001; Khairoutdinov and Randall 2006; Lima and Wilson 2008;

38 Khairoutdinov et al. 2009; Böing et al. 2012; Rowe and Houze 2015). The boundary between the

39 cold pool and the surrounding environmental air, known as the outflow boundary or gust front, is

40 key to sustaining multi-cellular deep convection (e.g. Weisman and Klemp 1986). It has also

41 been shown to trigger new convective cells in marine stratocumulus clouds (Wang and Feingold

42 2009; Terai and Wood 2013) and in trade-wind cumulus (Zuidema et al. 2012; Li et al. 2014).

43 Downdrafts also have implications for new particle formation in the outflow regions, which

44 contribute to maintaining boundary layer CCN concentrations in unpolluted environments (Wang

45 et al. 2016).

46   Precipitation-driven downdrafts are primarily a result of condensate loading and the

47 evaporation of hydrometeors in unsaturated air below cloud base (e.g. Houze 1993), with

48 evaporation thought to be the main driver (Knupp and Cotton 1985; Srivastava 1987). It was

49 originally suggested by Zipser (1977) that the downdrafts in the convective part of a system,

50 referred to in the literature as convective-scale downdrafts, are saturated and the downdrafts in

51 the trailing stratiform region (referred to as mesoscale downdrafts) are unsaturated. Studies with

52 large-eddy simulations (LES; Hohenegger and Bretherton 2011; Torri and Kuang 2016) indicate,

53 however, that most convective downdrafts are unsaturated, consistent with evidence that the

54 evaporation of raindrops within the downdraft likely does not occur at a sufficient rate to

55 maintain saturation (Kamburova and Ludlam 1966).

56   More recently, studies have shown the importance of downdraft parameters in

57 maintaining an accurate simulation of tropical climate in global climate models (GCMs;

58 Maloney and Hartmann 2001; Sahany and Nanjundiah 2008; Del Genio et al. 2012;

59   Langenbrunner and Neelin 2017). Accurate simulation of MCSs in continental regions (Pritchard

60   et al. 2011) was also shown to be sensitive to downdraft–boundary layer interactions, with

61   significantly improved representation of MCS propagation in the central US once such

62   interactions were resolved. Additionally, representing the effects of downdrafts and cold pools in

63   models has been shown to have positive effects on the representation of the diurnal cycle of

64   precipitation (Rio et al. 2009; Schlemmer and Hohenegger 2014).

65   This study aims to characterize downdrafts in a comprehensive way in the Amazon for

66   both isolated and mesoscale convective systems, and to provide useful guidance for downdraft

67   parameterization in GCMs. Data from the DOE–Brazil Green Ocean Amazon (GOAmazon)

68   campaign (2014–2015; Martin et al. 2016) provide an unprecedented opportunity to evaluate

69   downdraft characteristics in the Amazon with sufficiently large datasets for quantifying robust

70   statistical relationships describing leading order processes for the first time. Relationships

71   explored previously, primarily in tropical oceanic (Barnes and Garstang 1982; Feng et al. 2015;

72   de Szoke et al. 2017) or mid-latitude regions (Charba 1974; Engerer et al. 2008), such as time

73   composites of wind and thermodynamic quantities relative to downdraft precipitation, are also

74   revisited and compared to our findings over the Amazon. Downdrafts in MCSs and isolated cells

75   are compared to inform decisions concerning their unified or separate treatment in next

76   generation models. The effect of downdrafts on surface thermodynamics and boundary layer

77   recovery are examined, and the origin height of the downdrafts explored, combining inferences

78   from radar wind profiler data for vertical velocity and thermodynamic arguments from simple

79   plume models. Lastly, statistics describing cold pool characteristics at the surface are presented

80   and discussed for possible use as model diagnostics.

81   **2 Data and Methods**

82   Surface meteorological values (humidity, temperature, wind speed, precipitation) were

83   obtained from the Aerosol Observing meteorological station (AOSMET) at the DOE ARM site

84   in Manacapuru, Brazil, established as part of the GoAmazon2014/5 campaign. The record used

85   in this study spans 10 Jan 2014–20 Oct 2015. Values in this study are averaged at 30-min

86   intervals. Equivalent potential temperature is computed following Bolton (1980).

87   Thermodynamic profiles are obtained from radiosonde measurements within 6 h of a

88   convective event. Radiosondes are launched at approximately 01:30, 7:30, 13:30, and 19:30 LT

89   each day, with occasional radiosondes at 10:30 LT in the wet season. Profiles of vertical velocity

90 and radar reflectivity are obtained from a 1290 MHz radar wind profiler (RWP) reconfigured for

91 precipitation modes. It has a beam width of 6° (~ 1 km at 10 km AGL), a vertical resolution of

92 200 m, and a temporal resolution of 6 seconds (Giangrande et al. 2016).

93   Precipitation data at 25 km and 100 km, as well as convection classifications, are derived

94 from an S-Band radar located approximately 67 km to the northeast of the primary

95 GoAmazon2014/5 site (T3) at the Manaus Airport. Composite constant altitude low-level

96 gridded reflectivity maps (constant altitude plan position indicators, CAPPIs) were generated,

97 and the radar data were gridded to a Cartesian coordinate grid with horizontal and vertical

98 resolution of 2 km and 0.5 km, respectively. Rain rates were obtained from the 2.5 km

99 reflectivity using the reflectivity-rain rate (Z-R) relation $Z=174.8R^{1.56}$ derived from disdrometer

100 data. The spatially averaged rainfall rate over a 25 km and 100 km grid box were used in this

101 study. The center of the 100 km grid box is shifted slightly to the right of center with respect to

102 the T3 site due to reduced data quality beyond a 110 km radius.

103   All MCSs and isolated cells composited produce downdrafts that create a subsequent

104 drop in θ_e at the surface of more than 5 K in a 30-min period and have precipitation rates

105 exceeding 10 mm h^{-1} within that same period. These criteria were chosen to examine the most

106 intense downdraft events with the most well-defined vertical velocity signatures in the RWP

107 data. Only data for events with complete vertical velocity data coverage over the 1 h period

108 spanning the passage of the convective cells and centered around the maximum precipitation

109 were composited and evaluated.

110   Isolated convective cells were identified by S-Band composite reflectivity, as in Fig. 1,

111 and are defined as being less than 50 km in any horizontal dimension (contiguous pixels with

112 reflectivity > 30 dBZ) with a maximum composite reflectivity of greater than or equal to 45 dBZ.

113 Following the criteria defined above, this resulted in the selection of 11 events, all of which were

114 in the late morning or afternoon hours between 11:00 and 18:00 LT. Mesoscale convective

115 systems follow the traditional definition of regions of contiguous precipitation at scales of 100

116 km or greater (contiguous pixels with reflectivity > 30 dBZ) in any horizontal dimension (e.g.

117 Houze 1993; Houze 2004). All of the events sampled are characterized by a leading edge of

118 convective cells with a trailing stratiform region (Fig. 1), which is the most common MCS type

119 (Houze et al. 1990). The above criteria yielded 18 events: 11 in the late morning and early

120 afternoon hours (11:00-18:00 LT) and 6 in the late evening/early morning hours (22:00-11:00

121 LT).

122   In Sect. 6, statistics are presented using nearly the entire two-year timeseries of

123 meteorological variables at the GoAmazon2014/5 site, as well as 15 years of data (1996–2010)

124 from the DOE ARM site at Manus Island in the tropical western Pacific. One-hour averages are

125 computed in $\Delta\theta_e$ and precipitation.

126 **3 Surface Thermodynamics**

127   Composites of surface meteorological variables are displayed in Fig. 2 for the 11 isolated

128 cellular deep convective events coinciding with drops in equivalent potential temperature of 5 K

129 or greater and precipitation rates greater than 10 mm h^{-1} (see Sect. 2). The composites are

130 centered 3 h before and after the 5-min interval marking the sharpest decrease in surface θ_e in

131 the mean timeseries (time 0). All timeseries averaged in the composites are shifted to the mean

132 value at the θ_e minimum and shading on the composites shows +/- 1 standard deviation for

133 anomalies with respect to the θ_e minimum to provide a sense of the variability. All differences

134 quoted are the differences between the maximum and minimum values within the 1 h timeframe

135 of convective cell passage (+/- 30 min of time 0), unless noted otherwise. Recovery percentages

136 are computed as the difference between the minimum and maximum values between time 0 and

137 some specified time afterwards, divided by the difference between the minimum and maximum

138 values within 30 minutes of time 0.

139   In the two hours leading isolated convection, the CWV increases by 4.5 mm. The mean

140 value of θ_e 30 minutes before the minimum recorded θ_e are 353.7 K. As the systems pass, the θ_e

141 mean value drops by an average 9.6 K to an average value of 344.2 K. Since the isolated

142 convective cells observed occur in the daytime hours, the relative humidity is seen to drop

143 steadily throughout the 3 h period leading the convection following the rise in temperatures with

144 the diurnal cycle. The mean relative humidity (RH) rises to 82.3% within 30 minutes of system

145 passage, which indicates that the downdrafts are sub-saturated when they reach the surface.

146 Within the hour, temperatures drop by 4.2 K to 24.7 K, which is a smaller decrease than observed

147 over mid-latitude sites (see Table 2 in Engerer et al. 2008 for a review of mid-latitude case

148 studies) and specific humidity drops by 1.5 g kg^{-1} to 15.7 g kg^{-1}. Mean winds reach 6.4 m s^{-1},

149 consistent with previous studies that document strong horizontal winds associated with the

150   leading edges of cold pools (e.g. Fujita 1963; Wakimoto 1982), but are lower than the observed

151   values for mid-latitude storms (Engerer et al. 2008). Additionally, surface pressure often

152   increases with the existence of a cold pool and is referred to as the meso-high (Wakimoto 1982).

153   Here, it increases marginally by 0.6 hPa, but this value is much less than the typical values

154   observed in mid-latitudes (e.g. Goff 1976; Engerer et al. 2008). Lastly, 32.7% (52.4%) of the

155   temperature and 88.8% (88.9%) moisture depleted by the downdraft recovers within one (two)

156   hour(s) of cell passage, with moisture recovering more quickly and by a greater percentage than

157   temperature. It is likely that moisture recovers more quickly than temperature because of

158   increased evaporation, while cloud cover persistence may continue to affect temperature. It is

159   difficult to observe heat fluxes using eddy covariance techniques during precipitation, however,

160   so we are unable to properly quantify this. Nevertheless, we include measurements of heat fluxes

161   in Supplementary Figs. S1 and S2 to assess general trends.

162   Composites of surface meteorological variables are also shown in Fig. 2 for the 17 MCSs

163   with surface θ_e depressions of 5 K or greater and coincident precipitation rates of 10 mm h^{-1} or

164   greater. On average, the environment is more humid for MCSs than for the isolated cases, as is

165   seen in the CWV composite. CWV between hours -3 and -1 leading the MCSs is higher on

166   average than that observed leading the isolated cells, but increases to a comparable magnitude of

167   ~59 mm within the hour. CWV increases by an average of 1.5 mm in the 2 h leading the passage

168   of MCSs, which is slightly lesser than the increases reported in Taylor et al. 2017 (~4 mm) in the

169   Sahel, though the Amazon is a more humid environment. Values of θ_e leading the passage of

170   MCSs (350.3 K) are 3.4 K lower than the θ_e values leading the isolated cells (353.7 K), mostly

171   due to lower surface temperatures (27.0 K for MCSs vs. 28.9 K for isolated cells). The

172   precipitation occurs over a longer period than in the cases of isolated cells, as there is often

173   stratiform rain trailing the leading convective cells.   The stratiform rain and associated

174   downdrafts also sustain the cooling and drying of the near surface layers for many hours lagging

175   the precipitation maximum. The relative humidity maximum in the cold pool is 90.2% ($\Delta RH =$

176   13.3%), the specific humidity minimum is 15.4 g kg^{-1} (Δq = 1.6 g kg^{-1}), and the temperature

177   minimum is 22.8°C (ΔT = 4.2 K), with winds gusting to an average of 7.8 m s^{-1} with the passage

178   of the leading convective cells. The cold pools are thus cooler, drier, and nearer to saturation for

179   the MCSs than for the isolated cells. It is worth noting that these statistics for MCSs are not

180   greatly affected by the inclusion of nighttime events; composites for afternoon only MCSs yield

181 similar results. Overall, on average, the environments in which MCSs live are moister, they have

182 colder, drier cold pools that are nearer to saturation, the winds at their leading edges are gustier,

183 and the boundary layer recovers more slowly than for isolated cells.

184   Here, we composite events based on strict criteria identifying the strongest convective

185 events (see Table S1 for dates/times of events composited in Figs. 2-6). In Supplemental Figs. S1

186 and S2, we instead composite based on either a minimum θ_e decrease or a minimum

187 precipitation rate to test the sensitivity of the results presented here and include additional events.

188 We also examine the sensitivity to averaging by compositing timeseries of meteorological

189 variables averaged at 30-min intervals and plot results for 6 h leading and lagging the

190 convection. The features discussed above associated with the passage of isolated systems and

191 MCSs are generally robust to averaging and the choice of imposed criteria.

192 **4 Downdraft Origin and the Effects of Mixing**

193   Many previous studies of moist convective processes use θ_e as a tracer since it is

194 conserved in the condensation and evaporation of water and for dry and moist adiabatic

195 processes (e.g., Emanuel 1994). Tracing surface θ_e to its corresponding value aloft has been used

196 in many studies of tropical convection to examine potential downdraft origin heights (e.g. Zipser

197 1969; Betts 1973, 1976; Betts and Silva Dias 1979; Betts et al. 2002). This assumes that

198 downdraft air conserves θ_e to a good approximation and that downdraft air originates at one

199 height above ground level. Neither of these assumptions is likely to be true, as mixing is likely

200 occurring between the descending air and the environmental air and thus originating from

201 various levels. However, it can provide a useful reference point for further considerations.

202   We examine the mean θ_e profiles to place bounds on mixing and downdraft origin with

203 simple thermodynamic arguments and plume computations. The profiles composited in Fig. 3

204 were measured within the 6 hours prior to the same MCSs and isolated events composited in Fig.

205 2, less two MCS events that did not have corresponding radiosonde measurements. Simply

206 matching the mean of the minimum θ_e value within the cold pools to the minimum altitude at

207 which those values are observed yields 2.1 km for MCSs (left panel, Fig. 3) and 1.5 km for

208 isolated cells (right panel, Fig. 3). Again, this assumes that θ_e is conserved and that the air

209 originates at one altitude. If instead we assume that substantial mixing occurs with the

210 surrounding environment and that air originates at multiple levels in the lower troposphere, it

211 would be plausible for more of the air reaching the surface to originate at altitudes greater than
212 1.5 and 2.1 km for isolated cells and MCSs, respectively. This has been alluded to in previous
213 studies (e.g. Zipser 1969; Gerken et al. 2016), which provide evidence that air originates in the
214 middle troposphere.

215 To examine this, we mix air from above the altitude where the θ_e matched the surface
216 value (shown in the composites in Fig. 2) downward towards the surface, varying the
217 entrainment rate (constant in pressure coordinates). To start, we use a mixing of 0.001 hPa^{-1}, as
218 this is the constant entrainment value used in Brown and Zhang (1997) and Holloway and Neelin
219 (2009), which can produce realistic updraft buoyancy profiles over tropical oceans given
220 simplified assumptions about freezing (no freezing) and condensate loading (all condensate
221 retained). For the MCS case, it is plausible that a downdraft could originate at a height of 2.5 km
222 given this rate of mixing to reach the surface with characteristics given by Fig. 2. If instead the
223 air were coming from the level of minimum θ_e (≥ 3.2 km, on average), an assumption similar to
224 that made by many downdraft parameterizations (e.g. Zhang and McFarlane 1995; Tiedtke 1989;
225 Kain and Fritsch 1990), mixing would need be 2 times greater. For the isolated cells, mixing
226 rates appear to need to be greater in order to produce results consistent with cold pool
227 characteristics at the surface. If we start out at 0.002 hPa^{-1}, the rate sufficient for a minimum θ_e
228 origin for the MCSs, this only yields an origin height of 1.7 km. If instead we assume the air
229 originates somewhere near the level of minimum θ_e, mixing would need to be at least 0.004 hPa$^-$
230 ^{1}. For simplicity the discussion above is in terms of mean profiles – the standard error of the
231 profiles is shown at 50 mb intervals – but computation based on individual profiles yields a
232 standard error in the inferred mixing up about 0.0005 hPa^{-1}. For reference, in the European
233 Center for Medium Range Weather Forecasting Integrated Forecasting System (ECMWF IFS)
234 and Goddard Institute for Space Studies (GISS) Model E2 GCM (Kim et al. 2013), downdrafts
235 mix at a rate of 2 x 10^{-4} m^{-1} (roughly equivalent to 0.002 hPa^{-1} in pressure coordinates in the
236 lower troposphere).

237 To summarize, this analysis is suggestive of bounds on mixing coefficients for downdraft
238 parameterizations. If downdrafts of both convective types mix at similar rates, these results
239 suggest that downdrafts from isolated cells originate at lower levels than MCSs, on average. If
240 instead downdrafts originate from the level of minimum θ_e, mixing rates of 0.002 hPa^{-1} for
241 MCSs and 0.004 hPa^{-1} for isolated convection would be consistent with mean thermodynamic

242 conditions. In Sections 5 and 6, we provide a complementary probabilistic perspective on levels
243 of origin.

5 Vertical Velocity and Downdraft Probability

245   Figure 4 composites reflectivity (Z), vertical velocity (w), and the probability of
246 observing downdrafts (w < 0 m s^{-1}) for the 11 cases of isolated cellular convection meeting the
247 minimum $\Delta\theta_e$ criteria of -5 K and minimum precipitation criteria of 10 mm h^{-1}. Time 0 is the
248 time right before the sharpest decrease in θ_e and maximum precipitation (slightly offset from the
249 composites in Fig. 2). A 3 h window is composited for reference, but the interval of primary
250 interest is the 1 h window within which the minimum $\Delta\theta_e$ and maximum precipitation are
251 observed. To highlight the interval of interest, the 1 h intervals leading and lagging this period
252 are masked out.

253   The drop in θ_e is coincident with the passage of the isolated cell and its main updraft and
254 precipitation-driven downdraft. Mean reflectivity exceeding 40 dBZ is observed during this
255 period, as are strong updrafts in the middle-upper troposphere. The cell then dissipates and/or
256 moves past the site within an hour. A downdraft is observed directly below and slightly trailing
257 the updraft core. This is the downdraft that is associated with the largest drop in surface θ_e. As is
258 suggested in the literature, these are mainly driven by condensate loading and evaporation of
259 precipitation and are negatively buoyant. The probability of observing negative vertical velocity
260 (threshold < 0 m s^{-1}) within the 30 minutes of minimum $\Delta\theta_e$ and maximum precipitation is
261 highest in the lower troposphere (0-2 km), consistent with precipitation-driven downdrafts
262 observed in other studies (Sun et al. 1993; Cifelli and Rutledge 1994).

263   There is also a high probability of downdrafts in air near the freezing level (masked out in
264 the vertical velocity retrievals, as there is large error associated with retrievals near the freezing
265 level; Giangrande et al. 2016). It appears likely, however, that these downdrafts are
266 discontinuous in height more often than not, as high probabilities are not observed coincidentally
267 in the lowest levels beneath these downdrafts. These mid-upper level downdrafts are documented
268 in previous studies of MCSs, which suggest that they form in response to the pressure field (e.g.
269 Biggerstaff and Houze 1991), can occur quite close to the updraft (Lily 1960; Fritsch 1975), and
270 are positively buoyant (Fovell and Ogura 1988; Jorgensen and LeMone 1989; Sun et al. 1993).
271 These motions produce gravity waves in the stratosphere, as is discussed in Fovell et al. (1992).

272   Figure 5 shows the same composites for the 18 MCSs observed. They, too, have high

273   reflectivity (mean > 40 dBZ) in the 30 minutes coincident with the minimum θ_e and a defined

274   updraft extending up to the upper troposphere. Downdrafts occurring coincident with the

275   minimum θ_e are observed directly below the updraft signature in the mean vertical velocity

276   panel, and the probabilities are greatest below the freezing level. There are likely also mesoscale

277   downdrafts in the trailing stratiform region of the MCSs, although difficult to discern here, which

278   Miller and Betts (1977) suggest are more dynamically driven than the precipitation-driven

279   downdrafts associated with the leading-edge convection. These likely sustain the low θ_e air in

280   the boundary layer for hours after the initial drop, observed in Fig. 2. Vertical motions in the

281   stratiform region are weaker than in the convective region, and on average, as in Cifelli and

282   Rutledge (1994), rarely exceed 1 m s^{-1}.

283   Figure 6 is a concise summary of the results presented in Figs. 4 and 5, showing the mean

284   vertical velocity within the 30-min of sharpest $\Delta\theta_e$ for MCSs and isolated cells. Means are for w

285   > 0 m s^{-1} only (updrafts) or w < 0 m s^{-1} only (downdrafts) at each height (as in Giangrande et al.

286   2016) and are thus characteristic of magnitudes rather than bulk air motions. Updraft and

287   downdraft strength increases with height, consistent with results from previous studies evaluating

288   a broader range of conditions (May and Rajopadhyaya 1999; Kumar et al. 2015; Giangrande et

289   al. 2016). The corresponding mean probability of observing such motions at each height is

290   shown in the right panel. Probabilities, which can be interpreted loosely as convective area

291   fractions (Kumar et al. 2015; Giangrande et al. 2016), are largest below the freezing level for

292   downdrafts and in the 3-7 km region for updrafts. The probability of downdrafts for both isolated

293   cells and MCSs increases nearly linearly towards the surface below the freezing level. Thus, this

294   behavior in the lowest 3 km summarizes our results from the previous two figures and suggests

295   that the mean properties of downdrafts are such that air accumulates along descent – analogous

296   to mixing. The probability and vertical velocity for both MCSs and isolated cells correspond to

297   mass flux profiles that increase nearly linearly throughout the lower troposphere for updrafts and

298   that decrease nearly linearly throughout the lower troposphere for downdrafts, as seen in

299   Giangrande et al. (2016) over a broader range of convective conditions. To give some sense of

300   the error in these estimates, Wilson score intervals (lower bound/upper bound) for the 18 MCSs

301   cases are roughly 0.16/0.23 for a probability of 0.7, 0.21/0.21 for a probability of 0.5, and

302   0.23/0.16 for a probability of 0.3; for 11 events (as in the isolated cases), the intervals are

303 roughly 0.19/0.28 for a probability of 0.7, 0.25/0.25 for a probability of 0.5, and 0.28/0.19 for a

304 probability of 0.3.

305   These results, and those presented in the previous section, suggest a range of downdraft

306 origin levels throughout the lowest few kilometers within both organized and unorganized

307 convective systems. Several observational studies corroborate the evidence presented here that a

308 majority of the air reaching the surface in deep convective downdrafts originates at low-levels

309 (Betts 1976; Barnes and Garstang 1982; Betts et al. 2002; de Szoke et al. 2017). Betts (1976)

310 concluded that the downdraft air descends approximately only the depth of the subcloud layer

311 (~150 mb). Betts et al. (2002) cited a range of 765-864 hPa for the first levels at which the

312 surface θ_e values matched those of the air aloft. Additionally, there are many modeling studies

313 that provide evidence of these low-level origins (Moncrieff and Miller, 1976; Torri and Kuang,

314 2016). Recently, Torri and Kuang (2016) used a Lagrangian particle dispersion model to show

315 that precipitation-driven downdrafts originate at very low levels, citing an altitude of 1.5 km

316 from the surface, with the mode of the distribution nearer to 1 km. These conclusions are

317 consistent with our results here, suggesting that downdraft parameterizations substantially weight

318 the contribution of air from the lower troposphere (e.g. with substantial mixing and/or modifying

319 the height of downdraft origin).

320 **6 Relating Cold Pool Thermodynamics to Precipitation**

321   As seen in previous sections, the passage of both organized and unorganized convection

322 can lead to substantial decreases in θ_e resulting mainly from precipitation-driven downdrafts

323 formed from the leading convective cells. In this section, we search for robust statistical

324 relationships between key thermodynamic variables for potential use in improving downdraft

325 parameterizations in GCMs. These statistics differ from those presented in Figs. 2-6, as these

326 statistics are not conditioned on convection type and sample both precipitating and non-

327 precipitating points within the timeseries analyzed. All data available at the surface

328 meteorological station during the GoAmazon2014/5 campaign from 10 Jan 2014–20 Oct 2015

329 are included in these statistics.

330   The first of these statistics conditionally averages precipitation rate by $\Delta\theta_e$ (Fig. 7),

331 variants of which have been discussed in previous studies (Barnes and Garstang 1982; Wang et

332 al. 2016). Our statistics mimic those shown in previous work relating column-integrated moisture

333 to deep convection over tropical land (Schiro et al. 2016) and ocean (Neelin et al. 2009;

334 Holloway and Neelin 2009). The direction of causality in the CWV-precipitation statistics,

335 however, is the opposite of what is presented here. CWV is thought to primarily be the cause of

336 intense precipitation and deep convection, while here the $\Delta\theta_e$ observed is a direct result of the

337 precipitation processes and associated downdraft. Nevertheless, examining the distribution of

338 $\Delta\theta_e$ observed at the surface and magnitudes of the rain rates associated with the largest drops in

339 $\Delta\theta_e$ across different regions in the tropics can place bounds on downdraft behavior. We will also

340 conditionally average $\Delta\theta_e$ by precipitation rate, a more physically consistent direction of

341 causality.

342  Figure 7 shows precipitation rates binned by $\Delta\theta_e$ for in-situ and radar-derived

343 precipitation. Bins are 1 K in width (bins with less than 5 observations are eliminated from the

344 analysis) and precipitating events are defined as having rain rates greater than 2 mm h^{-1}. This

345 threshold is chosen based on results from Barnes and Garstang (1982), who suggested it as a

346 minimum precipitation rate for observing coincident decreases in θ_e at the surface. These

347 statistics mainly suggest that a majority of the substantial decreases in θ_e at the surface occur

348 coincidently with heavy precipitation, which is particularly evident from the sharp increase in

349 probability of precipitation (middle panel).

350  S-Band radar data are averaged in 25 km and 100 km grid boxes surrounding the

351 GoAmazon2014/5 site to examine the precipitation-$\Delta\theta_e$ relation with model diagnostics in mind

352 (Fig. 7). The $\Delta\theta_e$ shown is in situ, since we do not have spatial information in the moisture and

353 temperature fields at a high enough temporal frequency to match the radar data. Out to 25 km,

354 the statistics are very similar to those observed using in situ precipitation. Theoretical (Romps

355 and Jevanjee 2015), modeling (Tompkins 2001; Feng et al. 2015), and observational (Feng et al.

356 2015) studies have all examined typical sizes of cold pools, which can be on the order of 25 km

357 in diameter for any one cell. Cold pools can combine, however, to form a larger, coherent

358 mesoscale-sized cold pool (radius of 50 km or greater), as is commonly associated with

359 mesoscale convective systems (Fujita 1959; Johnson and Hamilton 1988). Therefore, it is likely

360 that our use of the in situ $\Delta\theta_e$, assuming cold pool properties are somewhat homogeneous in

361 space, is appropriate for scales up to 25 km. Beyond this scale, it is likely that the $\Delta\theta_e$ would be

362 smoothed by averaging, particularly for the smaller isolated cells, as would precipitation. For the

363 conditional average precipitation (Fig. 7), this effect may be seen at the 100 km averaging scale.

364   The probabilities are, however, robust to averaging. This suggests that when drops in θ_e occur

365   locally, there tends to be good correspondence to precipitation both locally and in the

366   surrounding 25 and 100 km averaging areas.

367   The width of the distribution of precipitating points is of greatest interest here. The

368   distribution of precipitating points peaks just shy of a $\Delta\theta_e$ of 0 K, indicating that most

369   precipitation events have low rain rates and do not occur coincidently with an appreciable drop

370   in θ_e. The frequency of precipitation drops off roughly exponentially towards lower $\Delta\theta_e$. An

371   interesting feature is the lower bound observed in $\Delta\theta_e$ near -15 K. The mean profiles in Fig. 3

372   show that, on average, this value of -15 K would be consistent with air originating from the level

373   of minimum θ_e and descending undiluted to the surface. The frequency of observing these values

374   suggests that air very rarely reaches the surface from these altitudes (3 km or higher) undiluted.

375   The θ_e probability distribution is consistent with the results of Sect. 5, indicating that the

376   probability of air from a given level of origin reaching the surface increases toward the surface

377   through the lowest 3 km.

378   Figure 8 shows remarkable similarity in these statistics when comparing across regions to

379   a DOE ARM site at Manus Island in the tropical western Pacific. As $\Delta\theta_e$ decreases, in situ

380   precipitation rates sharply increase. The PDFs, as well as the steepness and locations of the

381   pickups, are remarkably consistent. Again, the sharpness of these curves is a result of the

382   strongest precipitation events coinciding with the strongest decreases in θ_e, shown in the middle

383   panels in Fig. 8, where the probability of observing coincident precipitation is greatest at low

384    $\Delta\theta_e$.

385   It is then of interest to see if for a given precipitation rate we can expect a particular $\Delta\theta_e$,

386   as this is the proper direction of causality. Figure 9 conditionally averages $\Delta\theta_e$ by precipitation

387   rate (1-h averages). The minimum $\Delta\theta_e$ and maximum precipitation within a 3-h window are

388   averaged to minimize the effects of local precipitation maxima occurring slightly before or after

389   the maximum in $\Delta\theta_e$. Comparing Fig. 8 and Fig. 9 shows that there can be strong precipitation

390   events without large, corresponding decreases in surface θ_e, but that large decreases in surface θ_e

391   are almost always associated with heavy precipitation. Beyond about 10 mm h^{-1} there is a high

392   probability of observing large, negative $\Delta\theta_e$ and an apparent limit in mean θ_e decreases with rain

393   rate. This makes physical sense, as discussed above (see also Barnes and Garstang 1982), since

394   cooling is limited by the maximum difference between the surface θ_e and the θ_e minimum aloft.

395   The average $\Delta\theta_e$ for rain rates exceeding 10 mm h^{-1} is about -5 K for the Amazon and -4

396   K for Manus Island (Fig. 9). This statistic could be of use in constraining downdraft parameters

397   to be consistent with surface cooling and drying observed in nature. The results for 100 km

398   overlaid in Fig. 9 suggest that even though precipitation rates at 100 km are not simply

399   proportional to in situ rain rates, the main feature of the statistic is robust to averaging

400   precipitation out to a typical GCM grid scale. There are still, however, open questions about

401   scale dependence and how much cooling or drying should be observed for varying space and

402   time scales, given that we are using in situ $\Delta\theta_e$ for all of the statistics presented. Overall, if

403   convective precipitation is present in a GCM grid, a corresponding $\Delta\theta_e$ should result within a

404   range consistent to those observed here, subject to scale dependence.

405   To summarize the results from Figs. 7-9 and provide additional diagnostics, we can ask

406   what fraction of precipitation occurs within a given time window of an appreciable drop in θ_e,

407   and how this fraction changes with precipitation intensity. At the GoAmazon2014/5 site, for

408    $\Delta\theta_e \leq -2$ K, the fraction of precipitation events within the same hour exceeding 1, 5, 10 mm h^{-1},

409   respectively, is 43%, 63%, and 74%. Similar fractions (though smaller) are found at Manus Isl.:

410   37%, 53%, and 63%, respectively. Increasing the required value of $\Delta\theta_e$ yields smaller fractions –

411   e.g., for $\Delta\theta_e \leq -4$ K, corresponding fractions at the GoAmazon2014/5 site are about 75% of the

412   above values (37%, 53%, and 62%, respectively). Based on arguments presented above about

413   typical cold pool sizes, these result are likely applicable to GCM grid scales of 0.25° or less, with

414   evidence of consistency out to 1°.

415   **7 Conclusions**

416   Convective events sampled during the GoAmazon2014/5 campaign compare downdraft

417   characteristics between MCSs and isolated cells and examine their respective effects on surface

418   thermodynamics. All events included in the analysis passed directly over the GoAmazon2014/5

419   site with minimum precipitation rates of 10 mm h^{-1} and $\Delta\theta_e$ less than or equal to -5 K. The

420   isolated events sampled occurred in the afternoon hours only and were characterized by average

421   decreases of 1.5 g kg^{-1} in specific humidity, 4.2 K in temperature, and 9.6 K in θ_e, with an

422   increase of 4.2 m s^{-1} in wind speed at the surface. More than half (59%) of the deficit in θ_e

423   observed with the passage of the cells recovers within 1 h, on average, with the moisture

424   recovering faster than temperature and constituting a larger fraction of the total θ_e recovered.

425   MCSs show similar decreases in temperature (4.2 K), moisture (1.6 g kg^{-1}), and thus θ_e (9.7 K)

426   at the surface. The θ_e recovers more slowly for MCSs due to the mesoscale downdrafts and

427   associated precipitation in their trailing stratiform regions.

428   Vertical velocity profiles from a radar wind profiler show that the probability of

429   observing downdraft air during the 30 minutes of observed minimum $\Delta\theta_e$ increases with

430   decreasing height in the lowest 3 km for both isolated cells and MCSs. This vertical structure of

431   the downdraft probability is consistent with negative vertical velocities originating at various

432   levels within this layer and continuing to the surface. Considering complementary

433   thermodynamic arguments, without mixing, profiles of θ_e suggest that origin levels at average

434   altitudes of 1.4 and 2.1 km for isolated cells and MCSs, respectively, would be consistent with

435   average cold pool θ_e for these cases. A minimum in θ_e is observed between 3 and 7 km, on

436   average, so for air to originate above 3 km, simple plume calculations suggest that downdrafts in

437   MCSs would have to be mixing with environmental air at an approximate rate of 0.002 hPa^{-1}

438   along descent and at a rate roughly 2 times greater (0.004 hPa^{-1}) for isolated cells. This would

439   imply mass entering the downdraft throughout the lowest few kilometers. Overall the vertical

440   velocity and thermodynamic constraints are consistent in suggesting a spectrum of downdraft

441   mass origin levels throughout the lowest few kilometers.

442   Robust statistical relationships between $\Delta\theta_e$ and precipitation are examined from nearly

443   two years of data at the GoAmazon2014/5 site and 15 years of data at the DOE ARM site at

444   Manus Island in the tropical western Pacific. We conditionally average precipitation by $\Delta\theta_e$,

445   similar to the statistics of precipitation conditioned on a thermodynamic quantity we consider for

446   convective onset statistics. Here, however, the most likely direction of causality differs in that

447   the θ_e drop is caused by the downdraft that delivers the precipitation (as opposed to the

448   thermodynamic profile providing convective available potential energy for an updraft). For in

449   situ precipitation, the conditional average precipitation exhibits a sharp increase with decreasing

450   $\Delta\theta_e$, which is similar in magnitude over land and ocean, reaching roughly 10 mm hour^{-1} at a $\Delta\theta_e$

451   of -10 K. For area-averaged precipitation on scales typical of GCM grids, precipitation

452   magnitudes are smaller for strong, negative $\Delta\theta_e$, consistent with events with large $\Delta\theta_e$ occurring

453   at localized downdraft locations within a larger system with smaller area-average precipitation.

454   The probability distributions of $\Delta\theta_e$ (for precipitating and non-precipitating points) over land and

455   ocean are also remarkably similar. Distributions show exponentially decreasing probability with

456 decreasing $\Delta\theta_e$, providing additional evidence that downdraft plumes originating in the lowest

457 levels are orders of magnitude more likely than plumes descending with little mixing from the

458 height of minimum θ_e. Conditionally averaging $\Delta\theta_e$ by precipitation (the most likely direction of

459 causality) suggests an average limit in $\Delta\theta_e$ of -4 K to -5 K given high precipitation typical of

460 downdraft conditions. The corresponding 90th percentile yields $\Delta\theta_e$ of roughly -10 K, consistent

461 with results obtained from composting strong downdrafts. The robustness of these statistics over

462 land and ocean, and to averaging in space at scales appropriate to a typical GCM resolution,

463 suggests possible use of these statistics as model diagnostic tools and observational constraints

464 for downdraft parameterizations.

465 **Acknowledgments**

466   The U.S. Department of Energy Atmospheric Radiation Measurement (ARM) Climate

467 Research Facility GoAmazon2014/5 and Tropical West Pacific field campaign data were

468 essential to this work. This research was supported in part by the Office of Biological and

469 Environmental Research of the U.S. Department of Energy Grant DE-SC0011074, National

470 Science Foundation Grant AGS-1505198, National Oceanic and Atmospheric Administration

471 Grant NA14OAR4310274, and a Dissertation Year from the University of California, Los

472 Angeles Fellowship (KS). Parts of this material have been presented at the Fall 2016 meeting of

473 the American Geophysical Union and have formed part of K. Schiro's PhD thesis. We thank S.

474 Giangrande for providing RWP-derived vertical velocity and for helpful discussions.

475

476

477

478

479

480

481

482

483

484

485   **References**

486   Atmospheric Radiation Measurement (ARM) Climate Research Facility. 2013(a), updated

487   hourly. Meteorological Measurements associated with the Aerosol Observing System

488   (AOSMET). 2014-01-10 to 2015-10-20, ARM Mobile Facility (MAO) Manacapuru,

489   Amazonas, Brazil; MAOS (S1). Compiled by A. Koontz, J. Kyrouac and S. Springston.

490   Atmospheric Radiation Measurement (ARM) Climate Research Facility Data Archive:

491   Oak Ridge, Tennessee, USA. Data set accessed at http://dx.doi.org/10.5439/1025153.

492   Atmospheric Radiation Measurement (ARM) Climate Research Facility. 2013(b), updated

493   hourly. Balloon-Borne Sounding System (SONDEWNPN). 2014-01-10 to 2015-10-

494   20, ARM Mobile Facility (MAO) Manacapuru, Amazonas, Brazil; AMF1 (M1).

495   Compiled by D. Holdridge, J. Kyrouac and R. Coulter. Atmospheric Radiation

496   Measurement (ARM) Climate Research Facility Data Archive: Oak Ridge, Tennessee,

497   USA. Data set accessed at http://dx.doi.org/10.5439/1021460.

498   Atmospheric Radiation Measurement (ARM) Climate Research Facility. 2014, updated hourly.

499   Eddy Correlation Flux Measurement System (30ECOR). 2014-04-03 to 2015-10-20,

500   ARM Mobile Facility (MAO) Manacapuru, Amazonas, Brazil; AMF1 (M1). Compiled

501   by D. Cook. Atmospheric Radiation Measurement (ARM) Climate Research Facility

502   Data Archive: Oak Ridge, Tennessee, USA. Data set accessed at

503   http://dx.doi.org/10.5439/1025039.

504   Atmospheric Radiation Measurement (ARM) Climate Research Campaign Data, Observations

505   and Modeling of the Green Ocean Amazon (GOAMAZON), 2015. SIPAM Manaus S-

506   Band Radar. 10 Jan 2014–20 Oct 2015, 36° 3.1489^o S, 59.9914° W, Manaus, Amazonas,

507   Brazil (T1). Processed by C. Schumacher. Data set accessed Feb 2017

508   at iop.archive.arm.gov.

509   Atmospheric Radiation Measurement (ARM) Climate Research Facility Observations and

510   Modeling of the Green Ocean Amazon (GOAMAZON), 2015. Radar Wind Profiler

511   (1290RWPPRECIPMOM). Atmospheric Radiation Measurement (ARM) Climate

512   Research Facility Data Archive: Oak Ridge, Tenn. http://dx.doi.org/**10.5439/1256461**

513   Barnes, G. M. and M. Garstang, 1982: Subcloud Layer Energetics of Precipitating Convection.

514   *Monthly Weather Review*, **110**, 102-117.

515   Betts, A., 1973: Non-precipitating cumulus convection and its parameterization. *Quarterly*
516   *Journal of the Royal Meteorological Society*, **99**, 178-196.

517   Betts, A. K., 1976: The thermodynamic transformation of the tropical subcloud layer by
518   precipitation and downdrafts. *Journal of the Atmospheric Sciences*, **33**, 1008-1020.

519   Betts, A. K., and M. F. Silva Dias, 1979: Unsaturated downdraft thermodynamics in
520   cumulonimbus. *Journal of the Atmospheric Sciences*, **36**(6), 1061-1071.

521   Betts, A. K., and C. Jakob, 2002: Study of diurnal cycle of convective precipitation over
522   Amazonia using a single column model, *Journal of Geophysical Research.,* **107**, 4732.

523   Biggerstaff, M. I., and R. A. Houze Jr, 1991: Kinematic and precipitation structure of the 10–11
524   June 1985 squall line. *Monthly Weather Review*, **119**, 3034-3065.

525   Boing, S. J., H J. J. Jonker, A. P. Siebesma, and W. W. Grabowski, 2012: Influence of the
526   Subcloud Layer on the Development of a Deep Convective Ensemble. *Journal of the*
527   *Atmospheric Sciences,* **69**, 2682-2698.

528   Bolton, D., 1980: The computation of equivalent potential temperature. *Monthly Weather*
529   *Review*, **108**, 1046-1053.

530   Byers, H. R. and R. R. Braham, 1949: The thunderstorm: report of the Thunderstorm Project. *US*
531   *Government Printing Office.*

532   Cifelli, R., and S. A. Rutledge, 1994: Vertical motion structure in maritime continent mesoscale
533   convective systems: Results from a 50-MHz profiler. *Journal of the Atmospheric*
534   *Sciences*, **51**, 2631-2652.

535   Del Genio, A. D., Y. Chen, D. Kim, M.-S. Yao, 2012: The MJO Transition from Shallow to
536   Deep Convection in CloudSat/CALIPSO Data and GISS GCM Simulations. *Journal of*
537   *Climate,* **25**, 3755-3770.

538   Emanuel, K. A., 1994: Atmospheric Convection. 1st ed. Oxford University Press, 580 pp.

539   Engerer, N. A., D. J. Stensrud, and M. C. Coniglio, 2008: Surface characteristics of observed
540   cold pools. *Monthly Weather Review*, **136**, 4839-4849.

541   Feng, Z., S. Hagos, A. K. Rowe, C. D. Burleyson, M. N. Martini, and S. P. Szoeke, 2015:
542   Mechanisms of convective cloud organization by cold pools over tropical warm ocean
543   during the AMIE/DYNAMO field campaign. *Journal of Advances in Modeling Earth*
544   *Systems*, **7**, 357-381.

545   Fritsch, 1975: Cumulus dynamics: Local compensating subsidence and its implications for
546   cumulus parameterization. *Pure and Applied Geophysics,* **113***,* 851-867.

547   Fovell, R. G. and Ogura, Y., 1988: Numerical simulation of a midlatitude squall line in two
548   dimensions. *Journal of the Atmospheric Sciences*, **45**, 3846-3879.

549   Fovell, R., D. Durran, and J. R. Holton, 1992: Numerical simulations of convectively generated
550   stratospheric gravity waves. *Journal of the Atmospheric Sciences*, **49**, 1427-1442.

551   Fovell, R. G. and P. H. Tan, 1998: The temporal behavior of numerically simulated multicell-
552   type storms. Part II: The convective cell life cycle and cell regeneration. *Monthly*
553   *Weather Review*, **126**, 551-577.

554   Fujita, T., 1959: Precipitation and cold air production in mesoscale thunderstorm
555   systems. *Journal of Meteorology*, **16**, 454-466.

556   Gerken, T., D. Wei, R. J. Chase, J. D. Fuentes, C. Schumacher, L. Machado, R. V. Andreoli et
557   al., 2016: Downward transport of ozone rich air and implications for atmospheric
558   chemistry in the Amazon rainforest. *Atmospheric Environment,* **124**, 64-76.

559   Giangrande, S. E., T. Toto, M. P. Jensen, M. J. Bartholomew, Z. Feng, A. Protat, C. R. Williams,
560   C. Schumacher, and L. Machado, 2016: Convective cloud vertical velocity and mass-flux
561   characteristics from radar wind profiler observations during GoAmazon2014/5. *Journal*
562   *of Geophysical Research: Atmospheres*, **121**(21).

563   Goff, R., 1976: Vertical structure of thunderstorm outflows. *Monthly Weather Review*, **104**,
564   1429-1440.

565   Hohenegger, C. and C. S. Bretherton, 2011: Simulating deep convection with a shallow
566   convection scheme. *Atmospheric Chemistry and Physics*, **11**(20), 10389-10406.

567   Holloway, C. E., and J. D. Neelin, 2009: Moisture Vertical Structure, Column Water Vapor, and
568   Tropical Deep Convection. *Journal of the Atmospheric Sciences,* **66**, 1665–1683.

569   Houze, R. A., B. F. Smull, and P. Dodge, 1990: Mesoscale organization of springtime rainstorms
570   in Oklahoma. *Monthly Weather Review*, **118**, 613-654.

571   Houze, R.A., 1993: *Cloud Dynamics*, 573 pp., Academic, San Diego, Calif.

572   Houze, R. A., 2004: Mesoscale convective systems. *Reviews of Geophysics*, **42**(4).

573   Johnson, R. H., and P. J. Hamilton, 1988: The relationship of surface pressure features to the
574   precipitation and airflow structure of an intense midlatitude squall line. *Monthly Weather*
575   *Review*, **116**, 1444-1473.

576   Jorgensen, D. P. and M. A. LeMone, 1989: Vertical velocity characteristics of oceanic
577   convection. *Journal of the Atmospheric Sciences*, **46**, 621-640.

578   Kamburova, P. L. and F. H. Ludlam, 1966: Rainfall evaporation in thunderstorm
579   downdraughts. *Quarterly Journal of the Royal Meteorological Society*, **92**, 510-518.

580   Kain, J. S., and J. M. Fritsch, 1990: A one-dimensional entraining/detraining plume model and
581   its application in convective parameterization. *Journal of the Atmospheric Sciences*, **47**,
582   2784-2802.

583   Khairoutdinov, M., and D. Randall, 2006: High-resolution simulation of shallow-to-deep
584   convection transition over land, *Journal of the Atmospheric Sciences,* **63**, 3421 – 3436.

585   Khairoutdinov, M. F., S. K. Krueger, C. H. Moeng, P. A. Bogenschutz and D. A. Randall, 2009:
586   Large-eddy simulation of maritime deep tropical convection. *Journal of Advances in*
587   *Modeling Earth Systems*, **1**(4).

588   Knupp, K. R. and W. R. Cotton, 1985: Convective cloud downdraft structure: An interpretive
589   survey. *Reviews of Geophysics*, **23**, 183-215.

590   Kumar, V. V., C. Jakob, A. Protat, C. R. Williams, and P. T. May, 2015: Mass-flux
591   characteristics of tropical cumulus clouds from wind profiler observations at Darwin,
592   Australia. *Journal of the Atmospheric Sciences*, **72**, 1837–1855.

593   Langenbrunner, B. and J. D. Neelin: Multiobjective constraints for climate model parameter
594   choices: Pragmatic Pareto fronts in CESM1. *Journal of Advances in Modeling Earth*
595   *Systems*, accepted.

596   Li, Z., P. Zuidema, and P. Zhu, 2014: Simulated convective invigoration processes at trade wind
597   cumulus cold pool boundaries. *Journal of the Atmospheric Sciences*, **71**, 2823-2841.

598   Lily, D., 1960: On the theory of disturbances in a conditionally unstable atmosphere. *Monthly*
599   *Weather Review,* **88**, 1-17.

600   Lima, M. A., and J. W. Wilson, 2008: Convective storm initiation in a moist tropical
601   environment. *Monthly Weather Review*, **136**, 1847-1864.

602   Martin, S. T., P. Artaxo, L. A. T. Machado, A. O. Manzi, R. A. F. Souza, C. Schumacher, J.
603   Wang, M. O. Andreae, H. M. J. Barbosa, J. Fan, G. Fisch, A. H. Goldstein, A. Guenther,
604   J. L. Jimenez, U. Pöschl, M. A. Silva Dias, J. N. Smith, and M. Wendisch, 2016:
605   Introduction: Observations and Modeling of the Green Ocean Amazon
606   (GoAmazon2014/5). *Atmospheric Chemistry and Physics,* **16**, 4785-4797.

607 Maloney, E. D. and D. L. Hartmann, 2001: The sensitivity of intraseasonal variability in the
608   NCAR CCM3 to changes in convective parameterization. *Journal of Climate*, **14**, 2015-
609   2034.

610 May, P. T. and D. K. Rajopadhyaya, 1998: Vertical Velocity Characteristics of Deep Convection
611   over Darwin, Australia. *Monthly Weather Review*, **127**, 1056-1071.

612 Miller, M. J., and A. K. Betts, 1977: Traveling convective storms over Venezuela. *Monthly*
613   *Weather Review,* **105**, 833-848.

614 Moncrieff, M. W. and M. J. Miller, 1976: The dynamics and simulation of tropical
615   cumulonimbus and squall lines. *Quarterly Journal of the Royal Meteorological*
616   *Society*, **102**, 373-394.

617 Neelin, J.D., O. Peters, and K. Hales, 2009: The Transition to Strong Convection. *Journal of the*
618   *Atmospheric Sciences,* **66**, 2367–2384.

619 Pritchard, M. S., M. W. Moncrieff, and R. C. Somerville, 2011: Orogenic propagating
620   precipitation systems over the United States in a global climate model with embedded
621   explicit convection. *Journal of the Atmospheric Sciences*, **68**, 1821-1840.

622 Purdom, J. F., 1976: Some uses of high-resolution GOES imagery in the mesoscale forecasting
623   of convection and its behavior. *Monthly Weather Review*, **104**, 1474-1483.

624 Rotunno, R., J. B. Klemp, and M. L. Weisman, 1988: A Theory for Strong, Long-Lived Squall
625   Lines. *Journal of the Atmospheric Sciences,* **45**, 463–485.

626 Rio, C., F. Hourdin, J. Y. Grandpeix, and J. P. Lafore, 2009: Shifting the diurnal cycle of
627   parameterized deep convection over land. *Geophysical Research Letters*, **36**.

628 Romps, D. M., and N. Jeevanjee, 2016: On the sizes and lifetimes of cold pools. *Quarterly*
629   *Journal of the Royal Meteorological Society*, **142**, 1517-1527.

630 Rowe, A. K., and R. A. Houze, Jr., 2015: Cloud organization and growth during the transition
631   from suppressed to active MJO conditions. *Journal of Geophysical Research:*
632   *Atmospheres.,* **120**, 10324–10350.

633 Sahany, S. and R. S. Nanjundiah, 2008: Impact of convective downdrafts on model simulations:
634   results from aqua-planet integrations. In *Annales geophysicae: atmospheres,*
635   *hydrospheres and space sciences* (Vol. 26, No. 7, p. 1877).

636   Sahany, S., J. D. Neelin, K. Hales, and R. B. Neale, 2012: Temperature-moisture dependence of
637   the deep convective transition as a constraint on entrainment in climate models. *Journal*
638   *of the Atmospheric Sciences,* **69**, 1340–1358.

639   Schiro, K. A., J. D. Neelin, D. K. Adams, and B. R. Lintner, 2016: Deep Convection and Column
640   Water Vapor over Tropical Land versus Tropical Ocean: A Comparison between the
641   Amazon and the Tropical Western Pacific. *Journal of the Atmospheric Sciences*, **73**,
642   4043-4063.

643   Schlemmer, L., and C. Hohenegger, 2014: The Formation of Wider and Deeper Clouds as a
644   Result of Cold-Pool Dynamics. *Journal of the Atmospheric Sciences,* **71**, 2842–2858.

645   Srivastava, R. C., 1987: A model of intense downdrafts driven by the melting and evaporation of
646   precipitation. *Journal of the Atmospheric Sciences*, **44**, 1752-1774.

647   Sun, J., S. Braun, M. I. Biggerstaff, R. G. Fovell, and R. A. Houze Jr, 1993: Warm upper-level
648   downdrafts associated with a squall line. *Monthly Weather Review*, **121**(10), 2919-2927.

649   Terai, C. R. and R. Wood, 2013: Aircraft observations of cold pools under marine
650   stratocumulus. *Atmospheric Chemistry and Physics*, **13**(19), 9899-9914.

651   Tiedtke, M., 1989: A comprehensive mass flux scheme for cumulus parameterization in large-
652   scale models. *Monthly Weather Review*, **117**(8), 1779-1800.

653   Tompkins, A. M., 2001: Organization of tropical convection in low vertical wind shears: The
654   role of cold pools. *Journal of the Atmospheric Sciences,* **58**, 1650–1672

655   Torri, G. and Z. Kuang, 2016: A Lagrangian study of precipitation-driven downdrafts. *Journal of*
656   *the Atmospheric Sciences*, **73**(2), 839-854.

657   Wakimoto, R. M., 1982: The life cycle of thunderstorm gust fronts as viewed with Doppler radar
658   and rawinsonde data. *Monthly Weather Review*, **110**(8), 1060-1082.

659   Wang, H. and G. Feingold, 2009: Modeling mesoscale cellular structures and drizzle in marine
660   stratocumulus. Part I: Impact of drizzle on the formation and evolution of open
661   cells. *Journal of the Atmospheric Sciences*, **66**, 3237-3256.

662   Wang, J., R. Krejci, S. Giangrande, C. Kuang, H.M. Barbosa, J. Brito, S. Carbone, X. Chi, J.
663   Comstock, F. Ditas, and J. Lavric, 2016: Amazon boundary layer aerosol concentration
664   sustained by vertical transport during rainfall. *Nature,* **539**, 416-419.

665   Weisman, M. L., and J. B. Klemp, 1986: Characteristics of isolated convective storms.
666   In *Mesoscale Meteorology and Forecasting* (pp. 331-358). American Meteorological
667   Society.

668   Wilson, J. W., and W. E. Schreiber, 1986: Initiation of convective storms at radar-observed
669   boundary-layer convergence lines. *Monthly Weather Review*, **114**(12), 2516-2536.

670   Zhang, G. J., and N. A. McFarlane, 1995: Sensitivity of climate simulations to the
671   parameterization of cumulus convection in the Canadian Climate Centre general
672   circulation model. *Atmosphere-ocean,* **33**, 407-446.

673   Zipser, E. J., 1969: The role of organized unsaturated convective downdrafts in the structure and
674   rapid decay of an equatorial disturbance. *Journal of Applied Meteorology*, **8**, 799-814.

675   Zipser, E. J., 1977: Mesoscale and convective–scale downdrafts as distinct components of squall-
676   line structure. *Monthly Weather Review*, **105**, 1568-1589.

677   Zuidema, P., Z. Li, R. J. Hill, L. Bariteau, B. Rilling, C. Fairall, W. A. Brewer, B. Albrecht, and
678   J. Hare, 2012: On trade wind cumulus cold pools. *Journal of the Atmospheric
679   Sciences*, **69**, 258-280.

680

681

682

683

684

685

686

687

688

689

690   **Figures**
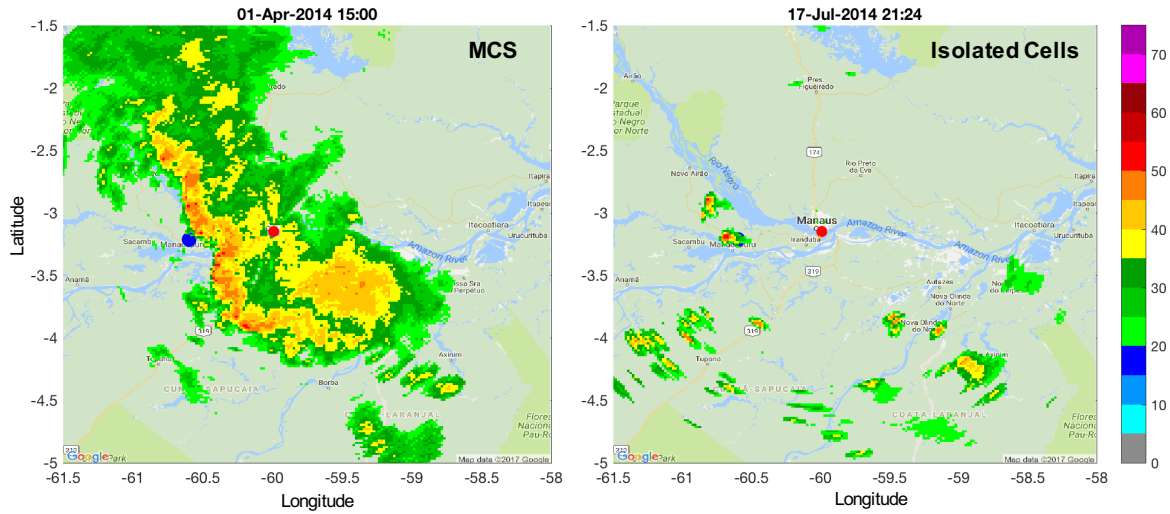
691

692   **Figure 1: Reflectivity (dBZ) from S-Band Radar on 01 Apr 2014 at 15:00 UTC (11:00 LT)**

693   **before the passage of an MCS, and at 17 Jul 2017 at 21:24 UTC (17:24 LT) after the**

694   **passage of an isolated cell. The red dot indicates the location of the S-Band radar, and the**

695   **blue dot indicates the location of the main GOAmazon site (T3).**
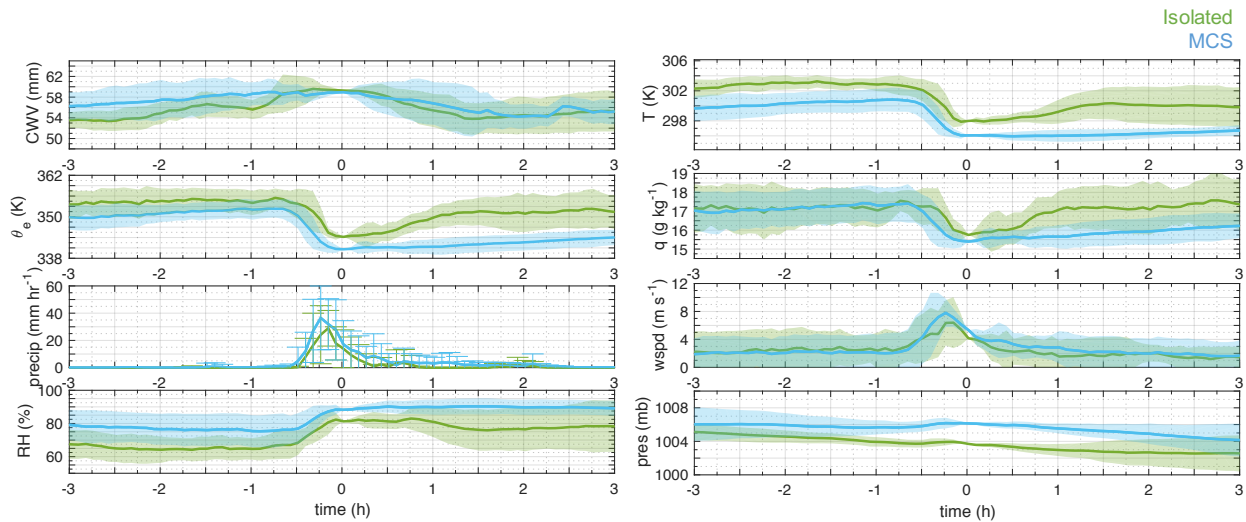
696

697   **Figure 2: Composites of meteorological variables from the AOSMET station at site T3 3 h**

698   **leading and 3 h lagging the minimum in equivalent potential temperature (0 h; 2nd panel)**

699   **coincident with the passage of isolated cells (green) and MCSs (blue). Shading denotes +/- 1**

700   **standard deviation of anomalies with respect to 0 h; bars on precipitation are +/- 1**

701 **standard deviation for each time interval. Standard errors would be smaller by a factor of**

702 **0.3 for isolated cells and 0.2 for MCSs.**
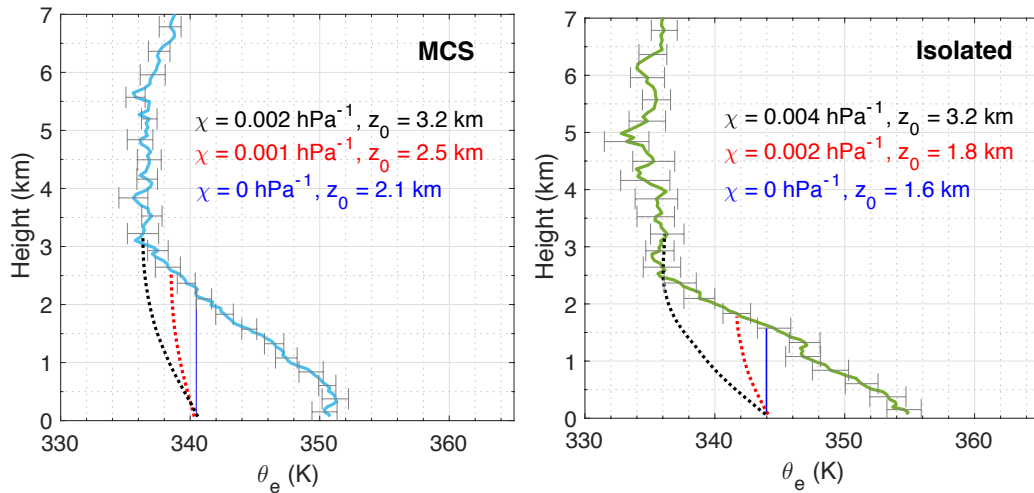
703

704 **Figure 3: Mean profiles of θ_e within 6 h leading the passage of a deep convective event for**

705 **MCSs (16 profiles; left) and isolated cells (11 profiles; right). Dashed lines indicate the**

706 **mean descent path for plumes originating at various altitudes and mixing with the**

707 **environment at various rates; solid blue line shows mean descent without mixing. Error**

708 **bars are +/- 1 standard error.**

709

710
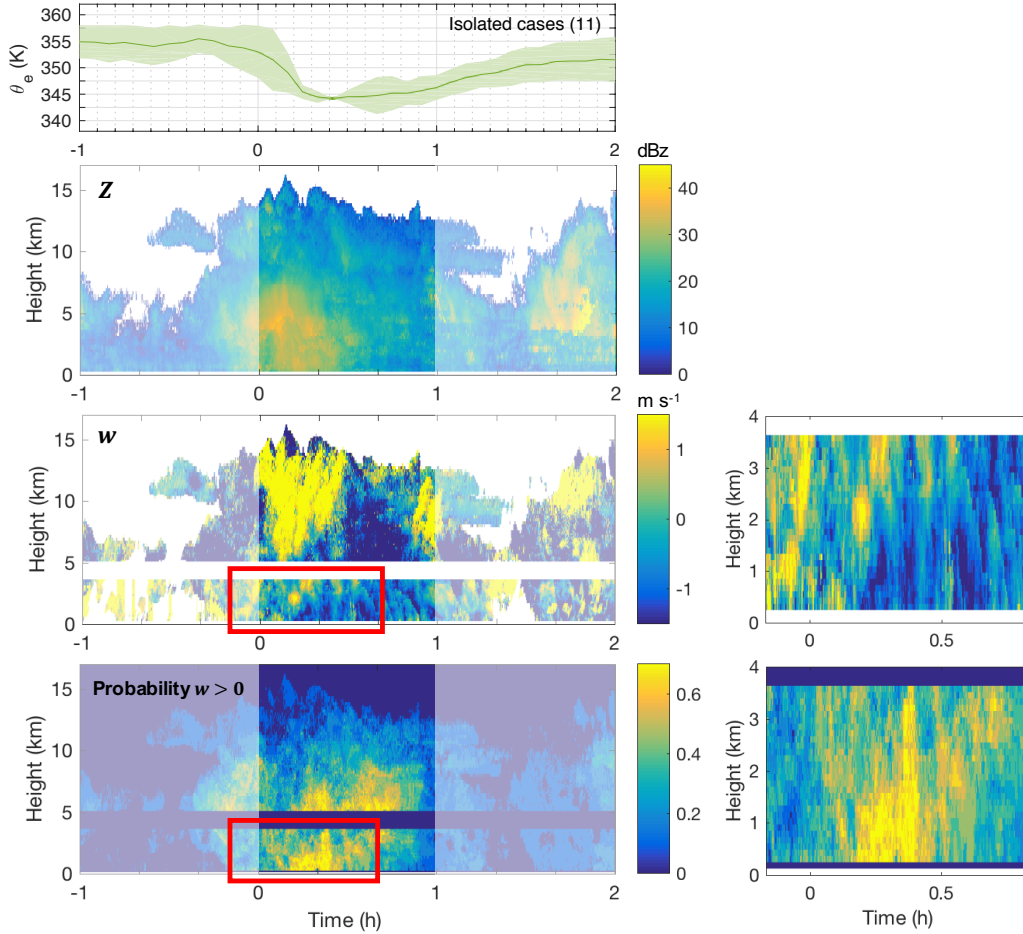
Figure 4: The composite θ_e (K; top panel), mean reflectivity (dBZ; second panel), mean vertical velocity (third panel; m s⁻¹), and probability of w < 0 m s⁻¹ (bottom panel) observed by the radar wind profiler at T3 leading and lagging the passage of isolated cells. Plots of w and probability zoomed in time and height (as outlined in red) are shown to the right of the corresponding plots for visual clarity.

716
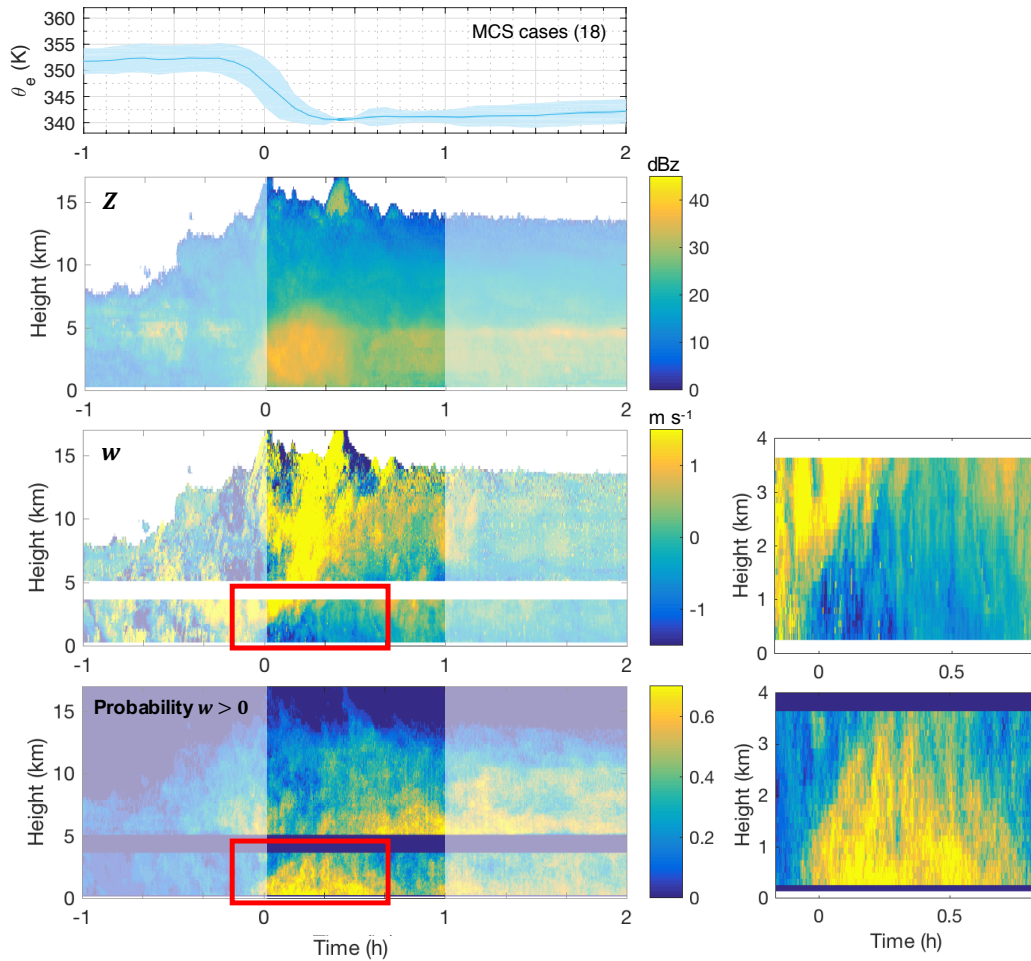
Figure 5: Same as Fig. 5, but leading and lagging the passage of MCSs.

718
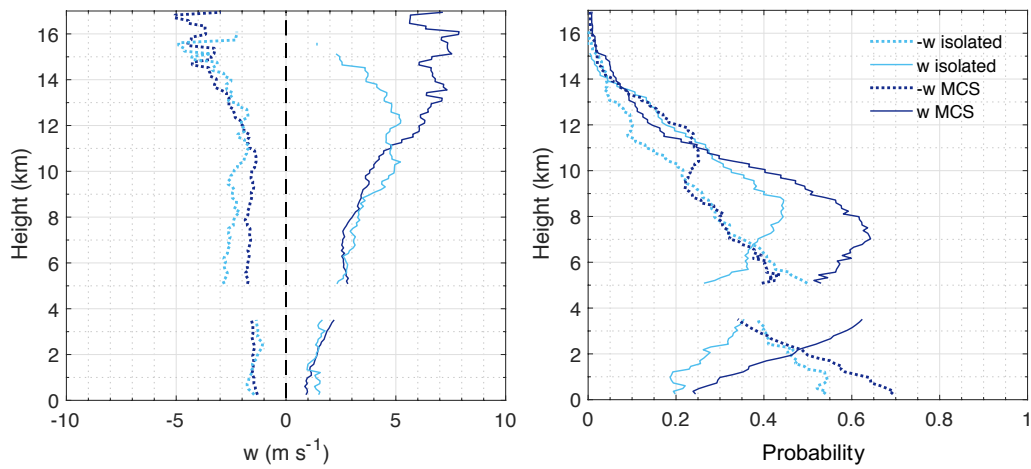
719

720 **Figure 6: (left) Mean vertical velocity profiles for MCSs and isolated cells for downdrafts**
721 **(w < 0 m s^{-1}; dashed) and updrafts (w > 0 m s^{-1}; solid). (right) Mean probability of**
722 **observing updrafts or downdrafts as a function of altitude. Means are composited from**
723 **data in the 30 minutes of largest drop in $\Delta\theta_e$ (0-0.5 h in Figs. 4 and 5).**

724
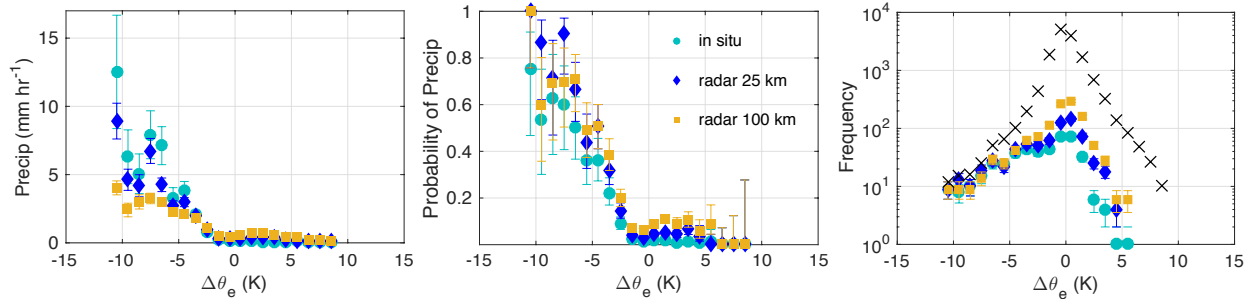
725
726 **Figure 7: (left) Precipitation (1-h averages) conditionally averaged by coincident changes in**
727 **equivalent potential temperature ($\Delta\theta_e$) at the GOAmazon site. Precipitation values**
728 **corresponds to the θ_e values at the end of each differencing interval. Bins are a width of 1°**
729 **and error bars represent the standard error. (middle) The probability of precipitation (> 2**
730 **mm h^{-1}) occurring for a given $\Delta\theta_e$. Error bars represent Wilson score intervals from 5-**
731 **95%. (right) The frequency of occurrence of $\Delta\theta_e$ and precipitation for a given $\Delta\theta_e$**
732 **(precipitation > 2 mm h^{-1}). Precipitation derived from S-Band radar reflectivity at spatial**
733 **averages over 25 km and 100 km grid boxes surrounding the GOAmazon site are included**
734 **for comparison to the in situ precipitation.**

735
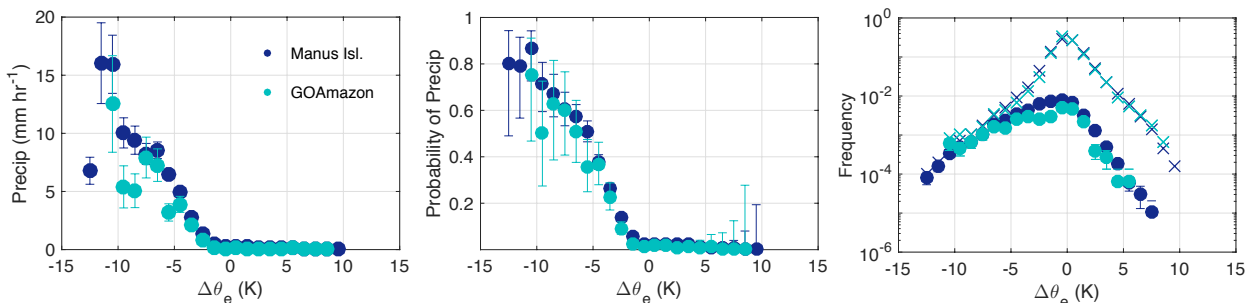
736
737 **Figure 8: Same as Fig. 7, except comparing results from in situ data only at the**
738 **GoAmazon2014/5 site (aqua) and the DOE ARM site at Manus Island (navy).**

739

740
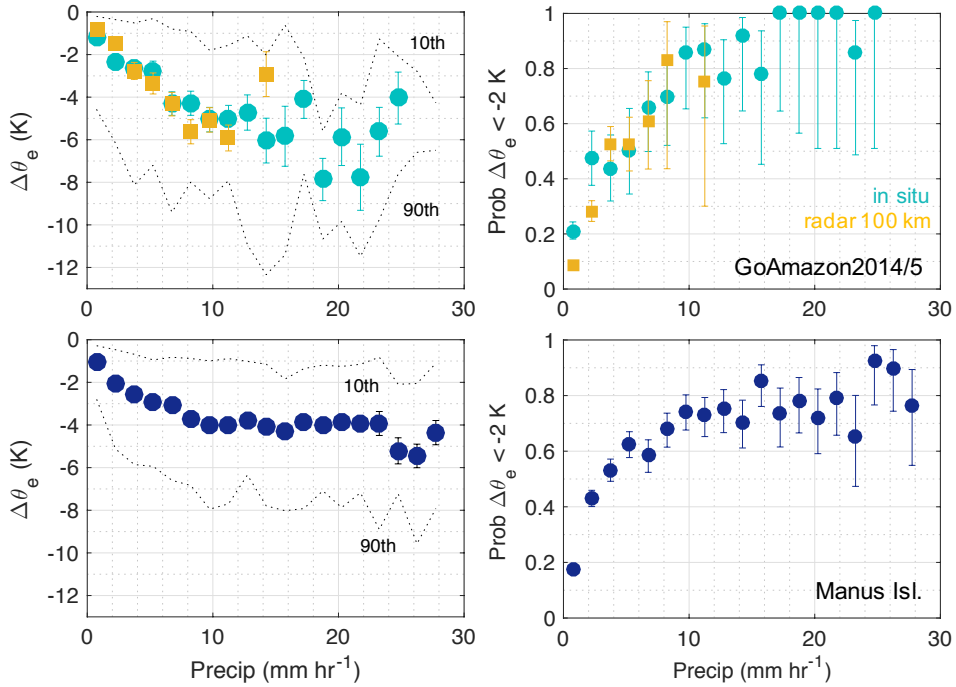
Figure 9: $\Delta\theta_e$ conditionally averaged by coincident precipitation (1-h averages) at the GOAmazon site (top) and at Manus Island (bottom). Precipitation values corresponds to the θ_e values at the end of each differencing interval. Bins are a width of 1.5 mm hr^{-1}. Error bars represent the standard error (left panels), and the 10th and 90th percentile values for each bin are drawn for reference (right panels). Error bars on the probability represent Wilson score intervals from 5-95%.

747